Ground and Excited States of [M(H_2timdt)$_2$] Neutral Dithiolenes (M = Ni, Pd, Pt; H_2timdt = Monoanion of Imidazolidine-2,4,5-trithione): Description within TDDFT and Scalar Relativistic (ZORA) Approaches

Pina Romaniello,[†] M. C. Aragoni,[‡] M. Arca,[‡] T. Cassano,[§] C. Denotti,[‡] F. A. Devillanova,[‡] F. Isaia,[‡] Francesco Lelj,*[,†] V. Lippolis,[‡] and R. Tommasi[§]

LAMI Dipartimento di Chimica and LASCAMM-INSTM Sezione Basilicata, Universitá della Basilicata, Via N. Sauro, 85100 Potenza, Italy, Dipartimento di Chimica Inorganica ed Analitica, S.S. 554 Bivio per Sestu, 09042 Monserrato-Cagliari, Italy, and Dipartimento di Fisica, Via G. Amendola 173, 1-70126 Bari, Italy

Received: March 25, 2003; In Final Form: July 6, 2003

Nonrelativistic and relativistic time-dependent density functional calculations have been performed on the excited states of the [M(H_2timdt)$_2$] (M = Ni, Pd, Pt) compounds. These complexes are characterized by an absorption at about $\lambda = 1000$ nm of rarely encountered intensity ($\epsilon \approx 8000$ M^{-1} cm^{-1}) compared to those of similar compounds, attributed to a $\pi \rightarrow \pi^*$ electronic transition between the HOMO and the LUMO. The comparison of the calculated spectra with the experimental data allows a possible assignment of the spectra. Our results confirm that, in all members of the series, the excited state at the lowest energy corresponds to a HOMO → LUMO excitation and indicate that a large number of the transitions have an *intraligand* character. No relevant direct relativistic effects can be observed on the pattern of the excited states and on energy differences between them as well. The main relativistic effect is due to the metal−sulfur bond contraction, which in contrast has considerable effect on the electronic structures.

1. Introduction

Since the first preparation in 1995 of some new neutral dithiolenes of formula [Ni(R_2timdt)$_2$] (R_2timdt = monoanion of dialkylimidazolidine-2,4,5-trithione], numerous [M(R,R′-timdt)$_2$] (M = Ni, Pd, Pt; R, R′ = alkyl or aryl) complexes have been synthesized and fully characterized.[1−4]

These planar complexes are characterized by several features peculiar to this class of compounds,[5] such as thermal and photochemical stability, existence of several reversible oxidation states, and intense vis−NIR absorption.[3,4] In particular, their UV−vis−NIR spectrum is dominated by an absorption located at about 1000 nm with unprecedented intensity ($\epsilon \approx 80\,000$ M^{-1} cm^{-1}).[4]

Both the metal and the R substituents affect the NIR absorption λ_{max} position, which can be tuned within the range 990−1030 nm. This NIR absorption candidates this class of dithiolenes as dyes for Q-switching and/or mode-locking the Nd:YAG laser ($\lambda = 1064$ nm) and the Nd:YLF laser ($\lambda = 1053$ nm), and in general for possible applications in the nonlinear optical field.[6]

An accurate description of the excited states of these dithiolenes and the comparison with the experimental data allow a possible assignment of the spectra. Furthermore, the analysis of the molecular orbitals (MOs) mainly involved in the transitions in terms of metal and ligand contributions shows the influence of the metal on the UV−vis−NIR spectra.

The pattern of excited states for the [M(H_2timdt)$_2$] [M = Ni (**1**), Pd (**2**), Pt (**3**)] complexes has been studied using time-dependent density functional theory (TDDFT).[7,8] This approach provides a first-principle method for calculating excitation energies and many response properties within a density functional context. Two approximations are made in TDDFT excitation energy calculations: the former is for the usual exchange-correlation (XC) potential v_{xc}, and the latter is for the XC kernel f_{xc} (the functional derivative of the XC potential with respect to the density).[9,10]

The relativistic effects[11,12] have been taken into account using a combined scalar relativistic (SR) ZORA[13−15] (zero-order regular approximation) and TDDFT approach.

2. Method and Computational Details

In the TDDFT framework, the excitation energies and oscillator strengths are obtained from the solution of the following eigenvalue equation:[7−9]

$$\Omega \mathbf{F}_i = \omega_i^2 \mathbf{F}_i \tag{1}$$

The components of the four-index matrix Ω are determined by the energies of the occupied and virtuals KS orbitals (ϵ_i, ϵ_j and ϵ_a, ϵ_b, respectively) and by the elements of the so-called coupling matrix **K**, containing Coulomb and XC parts:

$$\Omega_{ia\sigma,jb\tau} = \delta_{\sigma\tau}\delta_{ij}\delta_{ab}(\epsilon_a - \epsilon_i)^2 + 2\sqrt{(\epsilon_a - \epsilon_i)}K_{ia\sigma,jb\tau}\sqrt{(\epsilon_b - \epsilon_j)}$$

In eq 1, ω_i represents the excitation energy, while the oscillator strengths are obtained from the eigenvectors $\mathbf{F}_i$. According to Casida,[7] these eigenvectors can be used for an approximate description of the excited states. Here it is assumed that the single determinant of the KS orbitals is a reasonable approximation to the true ground-state wave function; the description is therefore based on KS orbitals.

* To whom correspondence should be addressed. E-mail: lelj@unibas.it.
[†] Universitá della Basilicata.
[‡] Dipartimento di Chimica Inorganica ed Analitica.
[§] Dipartimento di Fisica.

10.1021/jp034758r CCC: $25.00
Published on Web 10/17/2003

Two steps are involved in the TDDFT procedure: the SCF step, generating the KS orbitals and the respective energies, and the post-SCF step, solving eq 1. We have used the ALDA approximation for the post-SCF step, and we have employed both the BP (proposed by Becke[16] for the exchange and Perdew[17] for the correlation parts) and the asymptotically LB94 (by Van Leeuwen and Baerends)[18] exchange-correlation (XC) potentials for the XC potential which determines the KS orbitals and energies.

Relativistic calculations have been performed by combining the scalar relativistic (SR) ZORA[13] formalism with the TDDFT approach. This implies that the one-electron KS orbitals and their respective energies to be used in eq 1 are obtained by solving the one-electron (SR) ZORA Kohn−Sham equations.

For nonrelativistic calculations, we have used a valence triple-ζ STO basis set with two polarization functions for main element atoms (ADF V basis set)[19] and a triple-ζ *n*d, $(n + 1)$s basis with one $(n + 1)$p function for the metal (ADF IV basis set). The cores (C, N, 1s; S, Ni, 1s−2p; Pd,1s−3d; Pt,1s−4d) have been kept frozen.

For ZORA calculations, we have used an optimized valence basis set that is of the same size as the ADF V (IV for the metal) basis described above. The cores (C, N, 1s; S, Ni, 1s−2p; Pd, 1s−3d; Pt, 1s−4d) have been still kept frozen.

We have used both nonrelativistic and (SR) ZORA-optimized D_{2h} geometries of the complexes of the $[M(H_2timdt)_2]$ series. In the geometry optimization, the usual (nonrelativistic) BP density functional has been used.

The interaction between the two ionic ligands considered as a single bianionic fragment (L^{2-}) and the bivalent metal M^{2+} [M, $d_{x^2-y^2}{}^2 d_{z^2}{}^2 d_{xy}{}^0 d_{xz}{}^2 d_{yz}{}^2 (n+1)s^0$] has been investigated by using the fragments analysis proposed by Ziegler and Rauk.[20,21] The interaction energy (ΔE_{int}) is split into two physically meaningful terms:[22]

$$\Delta E_{int} = \Delta E^0 + \Delta E_{oi}$$

ΔE^0 is known as the steric repulsion energy, whereas the ΔE_{oi} term takes into account the attractive orbital interactions and can be split into the additive contributions from the various irreducible representations Γ of the overall symmetry group of the system. Among several possible formulations, the choice of these charged fragments has been considered the most suitable for describing the final ground-state bonding situation. In fact, this configuration has the advantage that the Pauli repulsion due to the $(n + 1)$s atomic orbital disappears and the empty nd_{xy} orbital acts as the acceptor orbital from the occupied ligand fragment $b_{1g}{}^L$ orbitals.

In addition, we have considered the effects of relativity both on the geometry of the complexes and on the KS−SCF energy.

3. Molecular Ground State and Electronic Structure of the $M(H_2timdt)_2$ Series

Geometries. Nonrelativistic and relativistic density functional geometry optimizations have been performed for the $[M(H_2timdt)_2]$ dithiolenes [M = Ni (**1**), Pd (**2**), Pt (**3**)] (Figure 1). UV−vis and NIR transitions have been computed at the relativistically optimized geometries.

To evaluate the best basis set and the best approximation to the ground-state XC functional, a preliminary study for the geometry of complex **1** has been performed: the basis set was varied from a single-ζ STO basis set frozen core up to an all-electron valence triple-ζ STO basis set with a single polarization function for the metal and two for other atoms. For the ground-state XC potential, we have used various approximations: the generalized gradient approximation (GGA) by Becke[16] for exchange and Perdew[17] for correlation (BP), the Vosko−Wilk−Nusair LDA potential,[23] and the Becke−Lee−Yang−Parr (BLYP) GGA.[16,24]

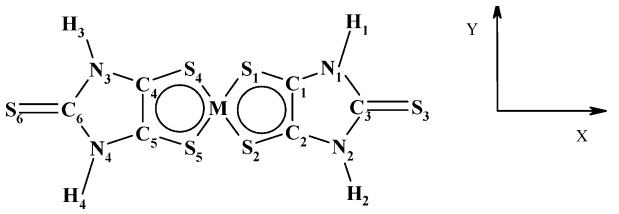

Figure 1. $[M(H_2timdt)_2]$ neutral model dithiolenes (M = Ni, **1**; Pd, **2**; Pt, **3**; H_2timdt = monoanion of imidazolidine-2,4,5-trithione).

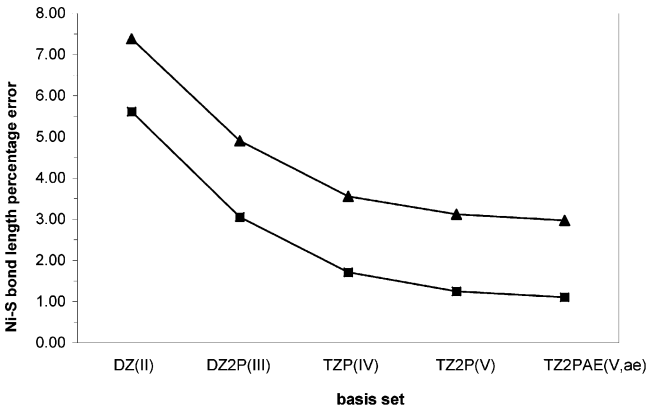

Figure 2. Percentage error for the nonrelativistic DFT (BLYP, ▲; BP, ■) Ni−S bond length (Å) in complex **1** with respect to the average experimental value determined for $[Ni(Me,Pr^i timdt)_2]$.[4]

The best agreement with experimental data[4] for $[Ni(Me,Pr^i timdt)_2]$ has been achieved using the BP XC potential together with a valence triple-ζ STO basis set with two polarization functions for main element atoms and a triple-ζ 3d,4s basis set with one 4p function for Ni and frozen cores (C, N, 1s; S, Ni, 1s−2p) (Figure 2).

Regarding the complexes with heavier metals, it has been necessary to take into account the relativistic effects in the geometry optimization. In particular, the nonrelativistic DFT Pd−S bond length is rather too long compared to experimental data for the $[Pd(Et_2timdt)_2]$, and the S−Pd−S bond angle is underestimated.

The most important relativistic effect on the geometry is related to the metal−sulfur bond length contraction. According to ZORA calculations, the bond length contraction is almost negligible for nickel, 0.010 Å, and increases to 0.027 Å for palladium and to 0.095 Å for platinum compared to the nonrelativistic optimized distances. Thus, according to ZORA geometry optimizations, the order in the metal−sulfur bond distances is Pd−S > Pt−S > Ni−S. The same trend is observed in the geometry optimizations with the Pauli formalism.[13] Without the relativistic bond contraction, the M−S bond length would increase monotonically along the series.

An analogous trend has been experimentally observed for $[M(edt)_2]$ complexes (M = Ni, Pd, Pt; edt = ethylenedithiolato; average distances 2.160, 2.305, and 2.297 Å on passing from Ni to Pt).[25]

Although we have no experimental data for the geometry of complex **3**, the relativistic Ni−S and Pd−S bond lengths are in good agreement with the experimental data found for $[Ni(Me,Pr^i timdt)_2]$ and $[Pd(Et_2timdt)_2]$ complexes, respectively (Table 1).[3,4]

TABLE 1: Theoretical M−S Bond Lengths (Å) and S−M−S Bond Angles (degrees) for the Model Compounds 1, 2, and 3 Compared with Those Reported for $[Ni(Me,Pr^i timdt)_2]$ and $[Pd(Et_2timdt)_2]$ Complexes[a]

	1		2		3	
method	Ni−S	S−Ni−S	Pd−S	S−Pd−S	Pt−S	S−Pt−S
NR DFT	2.190	94.53	2.350	91.18	2.411	89.58
(SR) ZORA	2.179	94.71	2.323	91.62	2.316	91.06
Pauli	2.178	94.74	2.316	91.76	2.296	91.44
exp[a]	2.163(1)	94.33(5)	2.295(2)	92.42(7)		

[a] Taken from refs 3 and 4. No structural characterization has been performed so far on $[Pt(R,R'timdt)_2]$ dithiolenes.

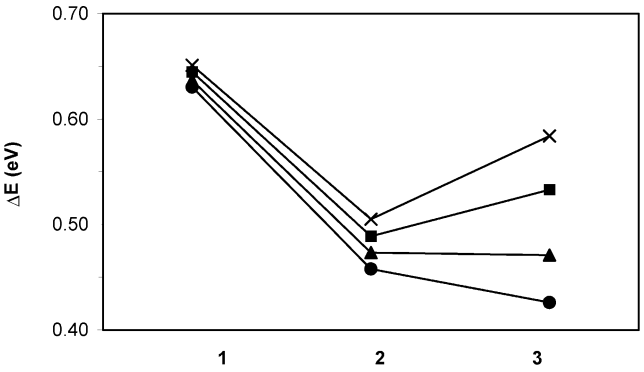

Figure 3. HOMO−LUMO energy gap ΔE (eV) calculated at nonrelativistic (NR, ●), relativistic SCF (RSCF, ▲), relativistic geometry (RG, ■) and RG+RSCF (×) levels. The basis set A (the IV and V ADF basis sets have been used for the metal and remaining atoms, respectively) and the corresponding ZORA basis set have been used for nonrelativistic and relativistic calculations.

The remaining bond lengths and bond angles show small changes among the members of the series and are not affected by relativistic corrections. The M−S bond contraction is very important for the trend of the HOMO−LUMO energy gap, which should follow the observed NIR excitation energy trend. Both nonrelativistic and relativistic values of the HOMO−LUMO gap at nonrelativistic geometries show an incorrect trend, i.e., the energy gap decreases along the series. In contrast, when the trend is calculated at relativistic geometries, it shows a minimum for complex **2**, as experimentally observed (Figure 3). This could be considered as an indirect proof of the validity of the relativistic contribution in determining the geometry of complex **3**.

Electronic Structure. Before dealing with the excited states of the $[M(H_2timdt)_2]$ series, it is useful to describe the ground-state electronic structure of these complexes, because the analysis of the energy and of the composition of the MOs is a good tool to get a first insight into the nature of the excited states. To this purpose, we present in Figure 4 the relativistic energy level scheme of the highest occupied and lowest unoccupied MOs of the $[M(H_2timdt)_2]$ series and in Figure 5 some MOs where the metal is mainly involved with the relative composition in terms of the M^{2+} and L^{2-} fragment orbitals (where L^{2-} indicates the two ionic ligands considered as a single bianionic fragment).

All the complexes have a closed-shell ground state. Considering the molecules lying in the *xy* plane, the HOMO is invariably the $5b_{1u}$ orbital, which is an almost pure ligand-π orbital, mainly localized on the np_z atomic orbitals of the sulfur atoms and carbon atoms of the dithiolenes core with a very low bonding contribution from the $(n+1)p_z$ atomic orbital of the metal, decreasing along the series (2.3%, 2.0%, and 1.8% for Ni, Pd, and Pt, respectively).

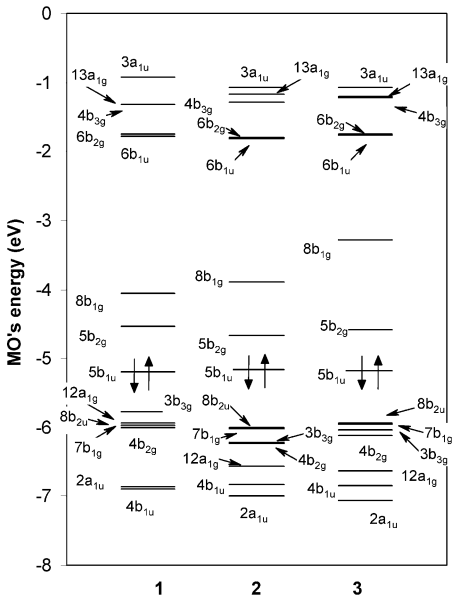

Figure 4. Relativistic energy level scheme for complexes **1**, **2**, and **3**. Only some selected frontier orbitals involved in the singlet transitions are reported. For the sake of homogeneity, the orbital numbering of complex **3** does not include the 4f valence orbitals of Pt.

The LUMO $5b_{2g}$ results from an antibonding interaction between the d_{xz} atomic orbital (10.2%, 6.8%, and 9.6% for Ni, Pd, and Pt, respectively) and the empty ligand-π $4b_{2g}{}^{L}$ (where the apex L refers to ligand fragment orbitals), mainly made up of the four np_z atomic orbitals of the sulfur donor atoms and, to a minor extent, the np_z of the carbon and exocyclic sulfur atoms. The mixing between the nd_{xz} atomic orbital and empty $b_{2g}{}^{L}$ ligand orbitals results in a small but not negligible π back-donation from the nd_{xz} atomic orbital into the $4b_{2g}{}^{L}$ orbital, which acquires a charge of 0.26, 0.20, and 0.24 e for Ni, Pd, and Pt, respectively. A larger contribution from the d_{xz} atomic orbital (39.9%, 18.2% and 19.6% for Ni, Pd and Pt, respectively) is found in the $4b_{2g}$ MO, resulting from an antibonding interaction with the full ligand-π $3b_{2g}{}^{L}$.

Metal−ligand π interactions involve the d_{yz} orbital, as well, in the b_{3g} representation.

In particular, the $3b_{3g}$ is an antibonding MO. Its bonding counterpart is the $2b_{3g}$, and the gap of the resulting π bonding/antibonding pair $2b_{3g}/3b_{3g}$ is ∼2 eV for the three complexes.

Since the d_{yz} orbital combines almost exclusively with occupied ligand-π orbitals, its charge depletion is negligible (1.94, 1.95, and 1.93 e for Ni, Pd, and Pt, respectively).

A noteworthy contribution from the metal (40.8%, 36.8%, and 39.0% nd_{xy} character for Ni, Pd, and Pt, respectively) is found in the $8b_{1g}$ orbital.

A significant d_{xy} character (37.2%, 26.9%, and 19.7% for Ni, Pd, and Pt, respectively) also occurs in the $6b_{1g}$ orbital (not reported in Figures 4 and 5), which is the bonding counterpart of the $8b_{1g}$ one. The large energy gap (∼4.6, 5.5, and 6.2 eV for Ni, Pd, and Pt, respectively) between the $8b_{1g}$ and the $6b_{1g}$ MOs, and the considerable population of the d_{xy} atomic orbital in all the complexes (1.13, 1.18, and 1.11 e for Ni, Pd, and Pt, respectively), are indicative of a strong metal−ligand σ interaction.

In fact, the Ziegler and Rauk energy analysis indicates the individual contribution $\Delta E^{B_{1g}}$ to the orbital interaction term ΔE_{oi} as the largest one (−1156.6, −1231.4, and −1172.4 kJ/mol with respect to the bonding energy of −3440.0, −3355.2, and −3495.6 kJ/mol for Ni, Pd, and Pt, respectively), in line with

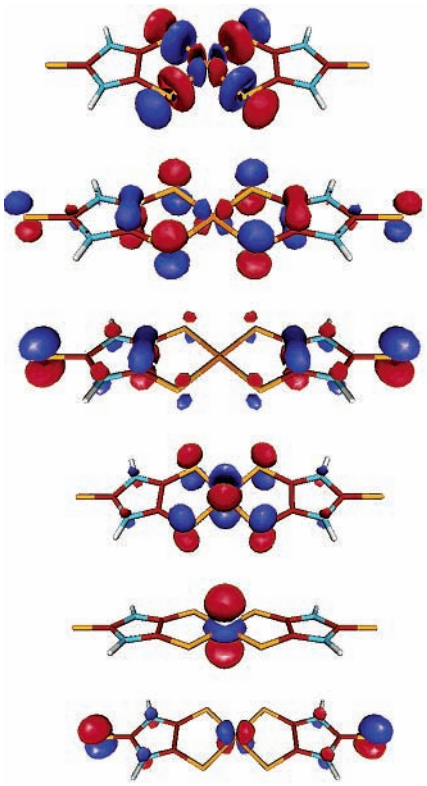

8 b_{1g} ⊃ nd_{xy} Ni: 40.8% Pd: 36.8% Pt: 39.0%

5b_{2g} ⊃ nd_{xz} Ni: 10.2% Pd: 6.8% Pt: 9.6%

5b_{1u} ⊃ $(n+1)p_z$ Ni: 2.3% Pd: 2.0% Pt: 1.8%

3 b_{3g} ⊃ nd_{yz} Ni: 67.4% Pd: 42.6% Pt: 44.3%

12 a_g⊃ nd_{z^2}, $(n+1)s$ Ni: 87.5%, 6.7% Pd:67.2%, 13.8% Pt:64.6%, 24.7%

4 b_{2g} ⊃ nd_{xz} Ni: 39.9% Pd: 18.2% Pt: 19.6%

Figure 5. Contribution of the metal-d atomic orbitals to the frontier molecular orbitals for **1**, **2**, and **3**.

the analyzed σ donation from the ligand to the M d_{xy} orbitals. In contrast, the orbital contributions $\Delta E^{B_{2g}}$ and $\Delta E^{B_{3g}}$, which account for the weaker π interaction, are negligible ($\Delta E^{B_{2g}} =$ −79.6, −101.9, and −110.5 kJ/mol; $\Delta E^{B_{3g}} =$ −44.5, −33.6, and −45.4 kJ/mol; both for Ni, Pd, and Pt, respectively).

The ΔE^{A_g} term contributes to the σ interaction as well (−307.4, −288.6, and −502.2 kJ/mol for Ni, Pd, and Pt, respectively). In particular, the $12a_g$ MO is an almost pure d_{z^2}, with a low contribution from the $(n + 1)$s atomic orbital and the $9a_g^L$ ligand orbital.

The mixing among the a_g-type orbitals induces a charge transfer from the filled d_{z^2} and $d_{x^2-y^2}$ atomic orbitals into the $(n + 1)$s orbital, whose population comes also from ligand-σ orbitals, in particular the $9a_g^L$ one (0.55, 0.49, and 0.85 e for Ni, Pd, and Pt, respectively). Probably the larger charge transfer for the Pt complex can be ascribed to the large relativistic stabilization of the $(n + 1)$s atomic orbital by the indirect effect of the largely filled relativistically expanded d valence shell. Indeed, the nonrelativistic atomic orbital population analysis indicates that just a charge of 0.51 e is transferred to the Pt−$(n + 1)$s orbital. As reported below, this relativistic effect is very important for the stability of Pt complex.

It is noteworthy that, according to the calculated MOs composition, among the MOs contributing to singlet transitions reported below, just the $8b_{1g}$, the $3b_{3g}$, the $12a_g$, and the $4b_{2g}$ MOs have large amplitudes on the metal. In contrast to these MOs, the HOMO ($5b_{1u}$) and the LUMO ($5b_{2g}$) have a predominant ligand character (Figure 5). The HOMO−LUMO energy gap is particularly interesting, since it can be related to the energy of the intense NIR transition,[4] which shows a minimum for the Pd complex.

As we have mentioned above, the correct trend is obtained at relativistic geometries, with only small increases in the energy gap when relativistic effects are included also at the SCF level (<0.05 eV).

As expected, the relativistic effects mostly affect the Pt complex; therefore, both in the RG and RG + RSCF calculations its HOMO−LUMO energy gap is larger than that calculated for the Pd complex. In the NR and RSCF calculations, the difference between the two energy gaps becomes almost negligible.

4. Electronic Spectra of the [M(H_2Timdt)$_2$] Series

The neutral [M(R,R′timdt)$_2$] (M = Ni, Pd, Pt) complexes are characterized by an intense absorption at about 1000 nm. In the series of the reported dithiolenes, both the metal and the R substituents affect the position of the NIR absorption, ranging between 990 and 1030 nm.[4]

We have referred to the UV−vis−NIR spectra of the [M(Et_2timdt)$_2$] (M = Ni, Pd, Pt) recorded in $CHCl_3$ solution for our excitation energy calculations and for the successive assignment of the spectra (Figure 6). Using their decomposition by means of Gaussian and Lorentzian curves, we have compared the experimental band maxima with calculated energies of transitions with significant oscillator strengths.

However, oscillator strength should be used rather qualitatively to distinguish allowed transitions from forbidden, very weak transitions to other excited states that also occur in the analyzed spectral regions.

Assignment of the Ni Complex Spectrum. To establish the influence of the chosen XC potential, we have compared the results obtained in the BP potential and in the LB94 potential for the most important transitions of complex **1**.

The compound belongs to the D_{2h} point group, the ground configuration being ^1A_g representation, and the pure electronic transitions $^1A_g \rightarrow {}^1B_{1u}$, $^1A_g \rightarrow {}^1B_{2u}$, and $^1A_g \rightarrow {}^1B_{3u}$ (*z*-, *y*-, and *x*-polarized, respectively) are orbitally and spin allowed.

Only the singlet−singlet excitation energies to the states belonging to the B_{2u} and B_{3u} representations are examined,

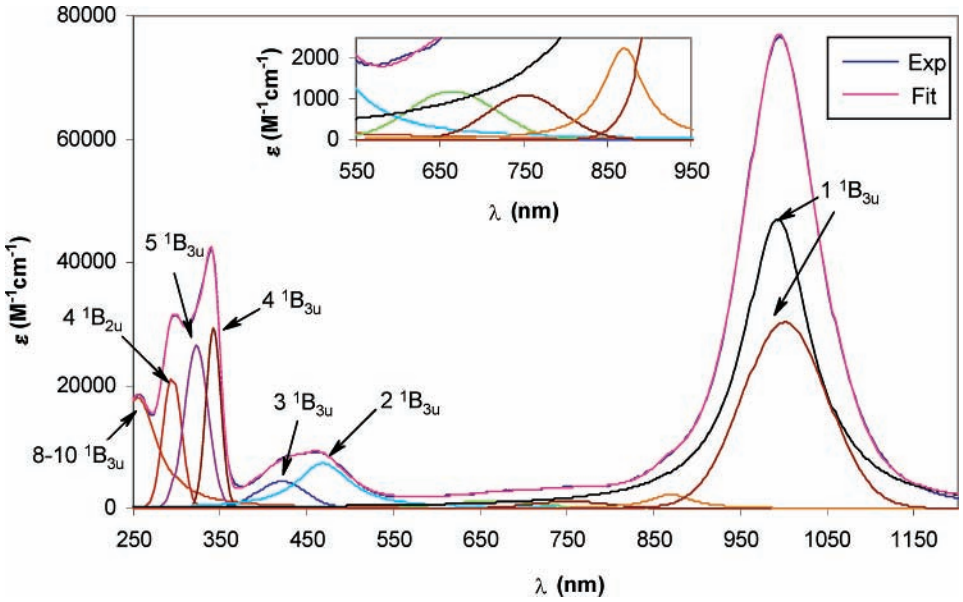

Figure 6. Experimental UV−vis−NIR spectrum of [Ni(Et_2timdt)$_2$] recorded in $CHCl_3$ solution and decomposition in Gaussian and Lorentzian curves. Assignments of the singlet configurations involved in the electronic transitions calculated by TDDFT are evidenced. The inset contains an enlargement of the region ranging between 550 and 950 nm.

TABLE 2: Excitation Energies (eV) Calculated for Complex 1 at LB94/ZORA and BP/ZORA Levels, along with the Value of $-\epsilon^{HOMO}$ [a]

state	LB94/ZORA	BP/ZORA
1^1B_{3u}	1.30 (0.20)	1.44 (0.38)
2^1B_{3u}	1.72 (0.26)	1.99 (0.18)
3^1B_{3u}	2.47 (0.08)	2.69 (0.06)
1^1B_{2u}	2.50 (0.00)	2.71 (0.01)
4^1B_{3u}	3.40 (0.51)	3.73 (0.43)
2^1B_{2u}	3.54 (0.04)	3.94 (0.01)
3^1B_{2u}	3.89 (0.00)	4.02 (0.00)
5^1B_{3u}	3.90 (0.49)	4.20 (0.51)
4^1B_{2u}	4.15 (0.13)	4.38 (0.12)
6^1B_{3u}	4.32 (0.05)	4.58 (0.10)
5^1B_{2u}	4.51 (0.00)	4.66 (0.00)
7^1B_{3u}	4.69 (0.04)	4.85 (0.15)
6^1B_{2u}	4.68 (0.00)	4.88 (0.04)
8^1B_{3u}	4.84 (0.13)	5.01 (0.01)
7^1B_{2u}	4.94 (0.00)	5.11 (0.00)
9^1B_{3u}	4.95 (0.08)	5.23 (0.03)
8^1B_{2u}	5.00 (0.01)	5.24 (0.00)
10^1B_{3u}	5.27 (0.11)	5.31 (0.00)
$-\epsilon^{HOMO}$	9.88	5.19

[a] Calculated oscillator strengths are given in parentheses.

because those relative to B_{1u} states have very small oscillator strengths. All the calculated spectra refer to relativistic calculation, described above. It is well-known that the LDA (or the standard GGA) potential gives remarkably good results for those states whose excitation energies are lower than $-\epsilon_{LDA}{}^{HOMO}$ (or $-\epsilon_{GGA}{}^{HOMO}$) and whose transitions do not involve a major contribution deriving from promotion to virtual orbitals too close to or above the threshold in the LDA (or GGA) potential.[26−29]

Thus, in Table 2, also the value of minus the orbital energy of the highest occupied KS orbital ($-\epsilon^{HOMO}$) is reported.

In our case, just a few calculated excitation energies in the BP potential are close to the $-\epsilon_{BP}{}^{HOMO}$ threshold, and these are not important for the assignment of the spectra.

In addition, the sensitivity of the energy of the bound virtual orbitals involved in the most important transitions with respect to the basis set has been investigated. The orbital energy has been calculated in the basis set used in the optimization (A) and in a basis set obtained by adding a set of one s, one p, and one d diffuse functions on the four sulfur donor atoms and on the four carbon atoms of the dithiolenes' core (since these atoms are mainly involved in the composition of the studied virtual orbitals), both in the BP and LB94 potentials (Table 3). The energy difference between consecutive virtual orbitals is similar in the two potentials. Furthermore, the orbital energies are not particularly sensitive to the radial extension of the basis set orbitals, suggesting that the selected virtual orbitals do not sample the long-range part of the potential.

TABLE 3: Selected KS Orbital Energies (eV) Calculated for Complex 1

functional	BP			LB94		
basis set	A	A,B		A	A,B	
orbital	$\epsilon_i{}^a$	$\epsilon_i{}^{a,b}$	$\epsilon_i - \epsilon_{i-1}{}^{a,b}$	$\epsilon_i{}^a$	$\epsilon_i{}^{a,b}$	$\epsilon_i - \epsilon_{i-1}{}^{a,b}$
$3a_u$	−0.94	−0.85	0.38	−5.86 ($13a_g$)[c]	−5.86	0.01
$13a_g$	−1.30	−1.23	0.03	−5.94 ($3a_u$)[c]	−5.87	0.34
$4b_{3g}$	−1.34	−1.26	0.44	−6.28	−6.21	0.54
$6b_{2g}$	−1.76	−1.70	0.03	−6.81	−6.75	0.02
$6b_{1u}$	−1.80	−1.73	2.29	−6.84	−6.77	2.03
$8b_{1g}$	−4.14	−4.02	0.45	−8.88	−8.80	0.42
$5b_{2g}$	−4.57	−4.47	0.63	−9.30	−9.22	0.59
$5b_{1u}$	−5.20	−5.10		−9.89	−9.81	

[a] The IV and V ADF basis sets have been used for the metal and remaining atoms, respectively. [b] One s, one p, and one d diffuse functions on the four sulfur and four carbon atoms of the dithiolenes core have been added. [c] The energy order of these two orbitals is inverse in the LB94 potential.

Thus, the difference between the excitation energies calculated with the BP potential and those calculated with the LB94 may be related to the different behavior of the two potentials in the inner region of the molecule.

An analogous analysis has been performed for **2** and **3** as well, confirming the above conclusions.

To analyze the experimental spectrum of [Ni(Et_2timdt)$_2$] dithiolenes, its decomposition by means of Gaussian and Lorentzian functions[30] has been performed. In particular, for the NIR peak both a Lorentzian curve and a Gaussian curve have been used, and the region ranging between 600 and 900 nm has been fitted by two Gaussian curves centered at 665 and 752 nm, respectively, and a Lorentzian one at 869 nm.

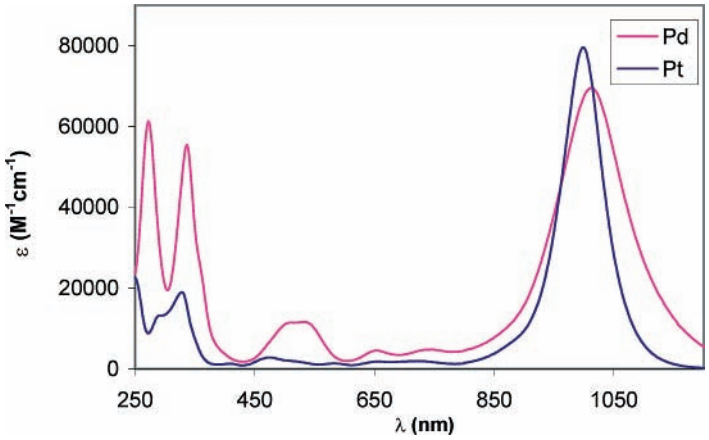

Figure 7. Experimental UV−vis−NIR spectrum of [M(Et_2timdt)$_2$] (M = Pd, Pt) recorded in $CHCl_3$ solutions.

In Figure 6, the experimental spectrum, its decomposition, and the assignment based on the calculated excitation energies with the largest oscillator strengths have been reported.

An examination of Figure 6 shows that the fitting functions correspond to calculated dipole transitions.

Present calculations show transitions falling in the region ranging between 550 and 950 nm, although they are symmetry-forbidden in the D_{2h} point group. However, the results calculated in the two potentials do not agree about the energy order of the mentioned excited states, not allowing an unambiguous assignment of these peaks. It is noteworthy that the two curves, fitting the NIR absorption peak, are both assigned to the same transition. In fact, our calculations do not reveal dipole-allowed transitions to excited states at energy lower than the 1^1B_{3u} one. Therefore, a possible suggestion for the NIR band assignment might refer the Lorentzian curve to the most important vibronic component of the electronic transition $^1A_g \rightarrow {}^1B_{3u}$, not necessarily the 0−0 one, whereas the additional Gaussian curve can be referred to the remaining components of the vibronic progression.

Both of the potentials used confirm the assignment of the intense NIR absorption, attributed to the HOMO → LUMO transition, although the excitation energy for this absorption is better described in the LB94 potential. Since the one-electron transition HOMO → LUMO contributes to the 1^1B_{3u} excited state with a percentage larger than 80%, this excited state has been optimized in a spin-unrestricted calculation. The most relevant geometry change associated with the electronic excitation to the 1^1B_{3u} excited state is the Ni−S bond stretching. Thus, vibrational modes involving the M−S bond might be mostly responsible for the mentioned vibronic structure. As a confirmation, it was previously pointed out, and will be thoroughly discussed in the section Vibrational Spectra, that the Nd:YAG laser excitation enhances just the metal−sulfur Raman-active bands.[2,4]

Our calculations suggest that the band at about 450 nm should be attributed to the two excitations 2^1B_{3u} and 3^1B_{3u}, although the 2^1B_{3u} has an excitation energy too low with respect to the experimental value. The peaks at 342 (3.62 eV), 322 (3.84 eV), and 295 nm (4.21 eV) could be mainly attributed to the 4^1B_{3u}, 5^1B_{3u}, and 4^1B_{2u} excitations, respectively.

Finally, the absorption at 255 nm (4.86 eV) cannot be unambiguously attributed since the LB94 and BP results do not agree on the excitation energies falling in this region. Hence, this band can be due to the transition to the 8^1B_{3u} excited state (and in part to the 10^1B_{3u} one), as calculated by the LB94 potential, or that to the $6B_{3u}$ and $7B_{3u}$ ones calculated by the BP potential (for the sake of simplicity, only the results calculated by the LB94 potential have been reported in Figure 6).

Regarding this mismatch, it is noteworthy that the excitation energies involved in the above-mentioned spectral region are close to the threshold $-\epsilon^{HOMO}$ in the BP potential, so the BP results could be not very reliable. On the other hand, the LB94 potential generally underestimates the excitations energies with respect to those calculated by the standard GGA potentials. The composition of both BP/ALDA and LB94/ALDA solution vectors points to a multiconfigurational character of the states under consideration. The compositions are similar in the two potentials; in particular, they present the same predominant transitions for the calculated states. Of particular interest is the excitation to the 8^1B_{3u} excited state, which, being dominated by the $3b_{3g} \rightarrow 3a_u$ one-electron transition, from a largely metal orbital (the $3b_{3g}$ with 67.4% $3d_{yz}$ character) to a pure ligand orbital, has a predominant metal-to-ligand charge-transfer (MLCT) character, with a minor *intraligand* contribution. Also in the solution vector for the 7^1B_{3u} and 9^1B_{3u} excited states, which have a predominant *intraligand* character, we find a non-negligible contribution (19% and 14%, respectively, in LB94) by the $3b_{3g} \rightarrow 3a_u$ transition.

The excitation to the 3^1B_{2u} excited state has a predominant MLCT character as well, due to the $3b_{3g} \rightarrow 6b_{1u}$ transition, in which the $6b_{1u}$ orbital is mainly localized on the ligand.

A partial MLCT character is also found in the excitations to the 7^1B_{2u}, 6^1B_{3u}, 4^1B_{3u}, 5^1B_{3u}, and 8^1B_{2u} states, although they have a prevalent *intraligand* character.

Finally, the excitations to the 2^1B_{3u}, 2^1B_{2u}, and 5^1B_{3u} states have a partial ligand-to-metal charge-transfer (LMCT) character because are dominated by transitions which are from nearly pure ligand orbitals ($8b_{2u}$, $10b_{3u}$, and $7b_{2u}$, respectively) to the $8b_{1g}$ orbital with a large, although not predominant, metal contribution (40.8% $3d_{xy}$ character).

All the transitions to the other calculated excited states have a predominant *intraligand* character.

Assignment of the Pd and Pt Complexes' Spectra. The spectra of Pd and Pt complexes are similar to the spectrum of the Ni complex (Figure 7). In particular, they are dominated by the very intense absorption at about 1000 nm, identified as a $\pi \rightarrow \pi^*$ transition, and by intense absorption bands in the 250−400 nm range.

The calculated dipole-allowed excitation energies and oscillator strengths of complexes **2** and **3** are reported in Tables 4 and 5, respectively, together with the values resulting from the decomposition of the experimental spectrum recorded for [Pd-

TABLE 4: Absorption Maxima Resulting from the Decomposition of the Experimental UV−Vis−NIR Spectrum of [Pd(Et_2timdt)$_2$] and TDDFT-Calculated Excitation Energies (eV) for Optically Allowed Excited States of Complex 3[a]

state	LB94/ZORA	BP/ZORA	LB94/NR	BP/NR	expt
1^1B_{3u}	1.21 (0.26)	1.31 (0.36)	1.19 (0.24)	1.28 (0.34)	1.23[b] (51025)
2^1B_{3u}	1.86 (0.13)	2.17 (0.10)	1.82 (0.14)	2.11 (0.11)	2.29 (8826)
3^1B_{3u}	2.35 (0.10)	2.55 (0.10)	2.34 (0.12)	2.54 (0.12)	2.50 (8028)
4^1B_{3u}	3.37 (0.50)	3.71 (0.50)	3.36 (0.54)	3.70 (0.56)	3.69 (42040)
5^1B_{3u}	4.09 (0.67)	4.40 (0.58)	4.07 (0.68)	4.36 (0.58)	4.56 (60309)
6^1B_{3u}	4.36 (0.00)	4.72 (0.00)	4.36 (0.00)	4.54 (0.00)	
7^1B_{3u}	4.61 (0.06)	4.80 (0.17)	4.60 (0.05)	4.79 (0.14)	
8^1B_{3u}	4.98 (0.31)	5.25 (0.22)	5.02 (0.34)	5.31 (0.23)	4.56 (60309)
9^1B_{3u}	5.12 (0.03)	5.40 (0.00)	5.16 (0.02)	5.43 (0.00)	
$-\epsilon^{HOMO}$	9.85	5.16	9.85	5.16	

[a] Molar absorptivities resulting from the decomposition of the experimental spectrum (M^{-1} cm^{-1}) and calculated oscillator strengths are given in parentheses; only the excitation energies to singlet excited states belonging to the B_{3u} symmetry have been reported. [b] Only the Lorentzian curve has been considered for the NIR band.

TABLE 5: Absorption Maxima Resulting from the Decomposition of the Experimental UV−Vis−NIR Spectrum of [Pt(Et_2timdt)$_2$] and TDDFT-Calculated Excitation Energies (eV) for Optically Allowed Excited States of Complex 2[a]

state	LB94/ZORA	BP/ZORA	LB94/NR	BP/NR	expt
1^1B_{3u}	1.33 (0.38)	1.41 (0.47)	1.28 (0.33)	1.36 (0.42)	1.24[b] (39641)
2^1B_{3u}	2.34 (0.08)	2.63 (0.01)	2.17 (0.10)	2.49 (0.06)	2.41 (1131)
3^1B_{3u}	2.45 (0.05)	2.71 (0.10)	2.39 (0.09)	2.60 (0.11)	2.64 (2083)
4^1B_{3u}	3.42 (0.33)	3.76 (0.34)	3.41 (0.44)	3.75 (0.45)	3.81 (17755)
5^1B_{3u}	4.24 (0.43)	4.58 (0.41)	4.24 (0.54)	4.56 (0.48)	4.29 (8312)
6^1B_{3u}	4.54 (0.04)	4.79 (0.06)	4.48 (0.12)	4.81 (0.03)	
7^1B_{3u}	4.79 (0.45)	5.11 (0.16)	4.70 (0.25)	4.93 (0.39)	4.96 (22241)
8^1B_{3u}	4.86 (0.18)	5.15 (0.47)	5.01 (0.26)	5.30 (0.11)	
9^1B_{3u}	5.08 (0.00)	5.28 (0.12)	5.17 (0.00)	5.40 (0.23)	
10^1B_{3u}	5.22 (0.33)	5.49 (0.24)	5.30 (0.34)	5.56 (0.27)	
$-\epsilon^{HOMO}$	9.87	5.17	9.88	5.18	

[a] Molar absorptivities resulting from the decomposition of the experimental spectrum (M^{-1} cm^{-1}) and oscillator strengths are given in parentheses; only the excitation energies to singlet excited states belonging to the B_{3u} symmetry have been reported. [b] Only the Lorentzian curves have been considered for the NIR band.

(Et_2timdt)$_2$] and [Pt(Et_2timdt)$_2$]. We have presented both the relativistic and nonrelativistic TDDFT calculations because relativistic effects are non-negligible with heavier metals.

It is noteworthy that the four sets of results do not show the same order (and compositions) of the excited states for both complexes. However, for the Pd complex, the four sets all agree on the lowest energy dipole-allowed transition (the HOMO → LUMO one) and on the principal states relevant for the spectrum assignment.

In the case of the Pt complex, the differences among the four sets of results are much more relevant. In this case also the results agree on the nature of excited states with larger oscillator strengths, and these are the same as those found for the Ni and Pd complexes. Only the promotion to the 7^1B_{3u} excited state features a large oscillator strength for the Pt complex by both the BP and LB94 potentials, whereas in the case of the other two complexes this configuration is not among the principal ones used in the spectra assignments based on the LB94 results. Furthermore, the 10^1B_{3u} excited state could contribute to the absorption at 250 nm (4.96 eV) just like in the case of complex **1**, although the composition is different.

The reasonable agreement between our results and experimental data for the Pd complex and the same assignment of the spectrum found for all the complexes may support the validity of the approach used.

In fact, the complexes show a similar composition of the most important excited states, at least as far as the same predominant components are concerned. Nevertheless, the 2^1B_{3u} and 3^1B_{3u} states of the Pt complex switch their composition in the BP potential, and the 5^1B_{3u} state is dominated by the $4b_{2g} \rightarrow 6b_{1u}$ transition, instead of the $7b_{2u} \rightarrow 8b_{1g}$ one calculated for Ni and Pd complexes.

Most of the calculated transitions involve MOs mainly localized on the ligand. Only the 8^1B_{3u} state and the 5^1B_{3u} and 2^1B_{3u} states show strong participation of a MLCT transition ($3b_{3g} \rightarrow 3a_u$) and a partial LMCT transition ($7b_{2u}/8b_{2u} \rightarrow 8b_{1g}$), respectively. Anyway, it is noteworthy that the $3b_{3g} \rightarrow 3a_u$ transition does not have a predominant MLCT character for the Pd and Pt complexes. In addition, since the 5^1B_{3u} state of the Pt complex is dominated by the $4b_{2g} \rightarrow 6b_{1u}$ transition, it has a non-negligible MLCT character.

5. Vibrational Spectra

To better characterize these complexes, their vibrational spectra have been analyzed.

The experimental IR spectra of the [M(R,R′timdt)$_2$] dithiolenes in the 3500−500 cm^{-1} region are practically superimposable, because they are characterized by bands relative to the ligand normal modes.

Much more interesting is the 50−500 cm^{-1} region (far-IR), where metal−sulfur vibrations are observed.

The far-IR spectra show two main bands: the most intense one falls at 435(2), 427(3), and 425(3) cm^{-1} for Ni, Pd, and Pt complexes, respectively; the latter falls at 380(2) and 339(2) cm^{-1} for Ni and Pd complexes, respectively, whereas it is not visible for the Pt complex.[4] The Raman spectra show only two very intense peaks at 330(4) and 434(1) cm^{-1} for the Ni complex, at 342(2) and 429(2) cm^{-1} for the Pd complex, and at 377(3) and 422(1) cm^{-1} for the Pt complex. [Note: These data refer to the average experimental vibrational frequencies recorded for [M(R,R′timdt)$_2$] dithiolenes reported in ref 4. The standard deviations have been reported in parentheses.]

DFT calculations can be useful to understand the nature and the type of these vibrational bands. We have calculated the

TABLE 6: Nonrelativistic (NR) and Relativistic (R) Vibrational Frequencies (cm^{-1}; IR Relative Intensities in Parentheses in km mol^{-1}) for Complexes 1, 2, and 3 Compared to the Average Experimental Vibrational Frequencies (cm^{-1}) Recorded for Several [M(R,R′timdt)$_2$] Dithiolenes

			expt			1		2		3	
mode		mode description[a]	Ni	Pd	Pt	NR	R	NR	R	NR	R
FIR	b_{3u}	S_2-M-S_1 $N_1-C_3-N_2$	435(2)	427(3)	425(3)	431 (120.7)	430 (126.1)	421 (164.9)	421 (161.1)	421 (157.6)	422 (173.0)
	b_{3u}	$M-S_1$	380(2)	339(2)	−	370 (43.7)	367 (38.6)	336 (8.8)	327 (14.9)	364 (17.5)	336 (5.2)
	b_{2u}	$M-S_1$				375 (7.0)	378 (5.8)	341 (5.9)	333 (6.8)	353 (6.2)	321 (5.8)
Raman	a_g	$M-S_1$	330(4)	342(2)	377(3)	334	332	340	336	382	369
	b_{1g}	$S_1-C_1-N_1$	434(1)	429(2)	422(1)	423	423	426	425	431	427
	a_g	S_2-M-S_1 $N_1-C_3-N_2$				429	429	425	426	429	428

[a] The assignments are in terms of the most relevant internal coordinates (all their related-symmetry internal coordinates are not reported for the sake of simplicity); all assignments involving three and two atoms are bending and stretching, respectively.

nonrelativistic and scalar relativistic ZORA vibrational spectra at ZORA-optimized geometries of the [M(H$_2$timdt)$_2$] complexes, with the same basis set used for the geometry optimizations and the BP approximation to the exchange correlation.

Table 6 reports a possible assignment of the bands described above.

Our calculations confirm the previous assignment[4] of the intense far-IR band, originating from the b_{3u} bending mode at 431, 421, and 421 cm^{-1} (at 430, 421, and 422 cm^{-1} in the relativistic calculations) for Ni, Pd, and Pt, respectively. The assignment of the two Raman peaks is confirmed as well, deriving from the a_g stretching mode at 334, 340, and 382 cm^{-1} (at 332, 336, and 369 cm^{-1} in the relativistic calculations) and from the big bending mode at 423, 426, and 431 cm^{-1} (at 423, 425, and 427 cm^{-1} in the relativistic calculations) or the a_g bending mode at 429, 425, and 429 cm^{-1} (at 429, 426, and 428 cm^{-1} in the relativistic calculations), respectively.

Regarding the second far-IR peak, it has been previously[4] assigned to a b_{2u} stretching mode. On the basis of the present calculations, it could originate from either the b_{2u} or the b_{3u} stretching mode at 375, 341, and 353 cm^{-1} (378, 333, and 321 cm^{-1} in the relativistic calculations) and at 370, 336, and 364 cm^{-1} (367, 327, and 336 cm^{-1} in the relativistic calculations). As already discussed, the experimental intensity of this band decreases along the series, and the same trend is followed by the relativistic intensities of the b_{3u} stretching mode, which are 38.6, 14.9, and 5.2 km mol^{-1} for the Ni, Pd, and Pt complexes, respectively. Therefore, the second far-IR peak can be attributed to the b_{3u} stretching mode instead of the b_{2u} one, as previously done.

6. Conclusions

Relativistic time-dependent density functional calculations have been performed on the excited state of the [M(H$_2$timdt)$_2$] (M = Ni, Pd, Pt) series. Theoretical results have been compared to the UV−vis−NIR spectra of [M(Et$_2$timdt)$_2$] dithiolenes and their decomposition in Gaussian and Lorentzian curves.

Our results, in particular those related to the Pd complex, are in very good agreement with experimental data. We have found that, in agreement with previous assignments, in all members of the [M(H$_2$timdt)$_2$] series the lowest excited state corresponds to the HOMO → LUMO transition, which has an *intraligand* character. All the calculated transitions show a prevalent *intraligand* character, which become stronger and stronger on passing from Ni to Pt. This is also the reason a large influence of the relativistic effects is not observed on the most important excited states, especially for the Pt complex.

On the other hand, relativistic effects are essential in order to reproduce correctly the geometry, in particular the M−S bond length trend, that shows a maximum value for the Pd complex, as expected.

The calculated nonrelativistic and relativistic vibrational spectra of the [M(H$_2$timdt)$_2$] (M = Ni, Pd, Pt) series confirm the previous assignment in the 50−500 cm^{-1} region. The second far-IR peaks, previously assigned to a b_{2u} stretching mode, can be instead attributed to the b_{3u} stretching mode on the basis of its relativistic intensity, which is in agreement with experimental data.

7. Experimental Section

Procedures and Methods. The syntheses of the [M(R,R′-timdt)$_2$] dithiolenes mentioned in this paper have been previously reported.[4] All solvents and reagents were Aldrich products, used as purchased. All operations were carried out under a dry nitrogen atmosphere. The degree of purity of each compound has been checked by CHNS and TLC analysis. Elemental analyses were performed on a FISONS EA-1108 CHNS-O instrument. Infrared spectra were recorded on a Bruker IFS55 spectrometer at room temperature, purging the sample cell with a flow of dried air. Polythene pellets with a Mylar beam-splitter and polythene windows (500−50 cm^{-1}, resolution 2 cm^{-1}), and KBr pellets with a KBr beam-splitter and KBr windows (4000−400 cm^{-1}, resolution 4 cm^{-1}), were used.

Electronic spectra were recorded with a cell of 1-cm optical path, on a Varian Cary 5 spectrophotometer in $CHCl_3$ solution at 20 °C in a thermostated compartment.

Computations. Quantum chemical calculations have been carried out by using the ADF2000 package.[31] Density functional theory (DFT) and time-dependent density functional theory (TDDFT) calculations have been performed by using BP (which uses the gradient correction proposed in 1988 by Becke for the exchange part along with the correlation term presented in 1986 by Perdew)[16,17] and LB94 (which refers to the XC potential of Van Leeuwen and Baerends)[18] functionals. The basis sets used for all nonrelativistic calculations are the ADF sets IV for metals and V for the remaining atoms, and those used for all relativistic calculations are the ZORA sets IV for metals and V for the other atoms (included in the ADF package).

The basis set superposition errors (BSSEs)[32] have been also calculated for all studied complexes. The BSSE corrections have a very small influence on the bonding energies and do not change the relative order in the bonding energies of the [M(H$_2$-timdt)$_2$] series (relativistic bonding energies corrected for BSSE,

−3405.7, −3356.8, and −3486.8 kJ/mol for **1**, **2**, and **3**, respectively).

Furthermore, the excited states of the [Ni(R,R′timdt)$_2$] dithiolenes (R = H, R′ = CH_3), with the two R′ groups in the trans position, have been calculated. This complex belongs to the C_{2h} point group, so some electronic transitions that are forbidden in the D_{2h} point group become accessible in this lower symmetry. Anyway, all the additional excited states show negligible oscillator strengths, confirming the good choice of the model complexes used in the present calculations.

Acknowledgment. Financial support through grants within "Legge 488-Cluster 14 Progetto operativo 8" within LASCAMM (Laboratorio per la Sintesi e la CAratterizzazione dei Materiali Molecolari) and MIUR PRIN (Progetti di Ricerca di Interesse Nazionale) is gratefully acknowledged.

References and Notes

(1) Bigoli, F.; Deplano, P.; Devillanova, F. A.; Lippolis, V.; Lukes, P. J.; Mercuri, M. L.; Pellinghelli, M. A.; Trogu, E. F. *J. Chem. Soc., Chem. Commun.* **1995**, 371.

(2) Bigoli, F.; Deplano, P.; Devillanova, F. A.; Ferraro, J. R.; Lippolis, V.; Lukes, P. J.; Mercuri, M. L.; Pellinghelli, M. A.; Trogu, E. F. *Inorg. Chem.* **1997**, *36*, 1218.

(3) Arca, M.; Demartin, F.; Devillanova, F. A.; Garau, A.; Isaia, F.; Lelj, F.; Lippolis, V.; Pedraglio, S.; Verani, G. *J. Chem. Soc., Dalton. Trans.* **1998**, 3731.

(4) Aragoni, M. C.; Arca, M.; Demartin, F.; Devillanova, F. A.; Garau, A.; Isaia, F.; Lelj, F.; Lippolis, V.; Verani, G. *J. Am. Chem. Soc.* **1999**, *121*, 7098.

(5) Mueller-Westerhoff, U. T.; Vance, B.; Yoon, D. I. *Tetrahedron* **1991**, *47*, 909.

(6) Wegnière, G. H. *Linear and Nonliner Optical Properties of Molecules*; Verlag Helvetica Chimica Acta: Base, Switzerland, 1993.

(7) Casida, M. E. Time-Dependent Density Functional Response Theory for Molecules. In *Recent Advances in Density Functional Methods*; Chong, D. P., Ed.; World Scientific: Singapore, 1995; Vol. 1, p 155.

(8) Casida, M. E. Time-Dependent Density Functional Response Theory of Molecular Systems: Theory, Computational Methods, and Functionals. In *Recent Developments and Applications of Modern Density Functional Theory*; Seminario, J. M., Ed.; Elsevier: Amsterdam, 1996.

(9) van Gisbergen, S. J. A. Molecular Response Property Calculations Using Time-Dependent Density Functional Theory. Ph.D. Thesis, 1998 (available online at http://www.scm.com).

(10) van Gisbergen, S. J. A.; Koostra, F.; Schipper, P. R. T.; Gritsenko, O. V.; Snijders, J. G.; Baerends, E. J. *Phys. Rev. A* **1998**, *57*, 2556.

(11) Pyykkö, P. *Chem. Rev.* **1988**, *88*, 563.

(12) van Wezenbeek, E. Relativistic effects in Atoms and Molecules. Ph.D. Thesis, 1992 (available online at http://www.scm.com).

(13) van Lenthe, E. ZORA. Ph.D. Thesis, 1996 (available online at http://www.scm.com).

(14) van Lenthe, E.; Baerends, E. J.; Snijders, J. G. *J. Chem. Phys.* **1993**, *99*, 4597. van Lenthe, E.; Baerends, E. J.; Snijders, J. G. *J. Chem. Phys.* **1994**, *101*, 9783.

(15) van Lenthe, E.; Baerends, E. J.; Snijders, J. G. *J. Chem. Phys.* **1994**, *101*, 9783.

(16) Becke, A. *Phy. Rev. A* **1988**, *38*, 3098.

(17) Perdew, J. P. *Phys. Rev. B* **1986**, *33*, 8822.

(18) van Leeuwen, R.; Baerends, E. J. *Phys. Rev. A* **1994**, *49*, 2421.

(19) ADF STO basis set database available on line at http://www.scm-.com.

(20) Ziegler, T.; Rauk, A. *Theor. Chim. Acta* **1977**, *46*, 1.

(21) Ziegler, T.; Rauk, A. *Inorg. Chem.* **1979**, *18*, 1558.

(22) Ziegler, T. In *Metal−Ligand Interations: From Atoms, to Clusters, to Surfaces*; Salahub, D. R., Russo, N., Eds.; NATO ASI Series 378; Kluwer Academic Publishers: Dordrecht, The Netherlands, 1992; p 367.

(23) Vosko, S. H.; Wilk, L.; Nusair, M. *Can. J. Phys.* **1980**, *58*, 1200.

(24) Lee, C.; Yang, W.; Parr, R. G. *Phys. Rev. B* **1988**, *37*, 785.

(25) Schrauzer, G. N.; Mayweg, V. P. *J. Am. Chem. Soc.* **1965**, *87*, 3582. Browall, K. W.; Bursch, T.; Interrante, L. V.; Kasper, J. S. *Inorg. Chem.* **1972**, *11*, 1800. Schlaipfer, C. W.; Nakamoto, K. *Inorg. Chem.* **1975**, *14*, 1338.

(26) Casida, M. E.; Jamorski, C.; Casida, K. C.; Salahub, D. R. J. *Chem. Phys.* **1998**, *108*, 4439.

(27) Bauernschmitt, R.; Ahlrichs, R.; Hennrich, F. H.; Kappes, M. M. *J. Am. Chem. Soc.* **1998**, *120*, 5052−5059.

(28) Casida, M. E.; Salahub, D. R. *J. Chem. Phys.* **2000**, *113*, 8918.

(29) Schipper, P. R. T.; Gritsenko, O. V.; van Gisbergen, S. J. A.; Baerends, E. J. *J. Chem. Phys.* **2000**, *112*, 1344.

(30) Aragoni, M. C.; Arca, M.; Crisponi, G.; Nurchi, V. M. *Anal. Chim. Acta* **1995**, *316*, 195.

(31) Fonseca Guerra, C.; Visser, O.; Snijders, J. G.; te Velde, G.; Baerends, E. J. Parallelisation of the Amsterdam Density Functional Program. In *Methods and Techniques of Computational Chemistry*; Clementi, E., Corongiu, G., Eds.; STEF: Cagliari, 1995.

(32) Boys, S. F.; Bernardi, F. *Mol. Phys.* **1970**, *19*, 553.